A Multi-Scale Algorithm for three dimensional Free Hand Ultrasound

João M. Sanches Jorge S. Marques

Instituto Superior Técnico / Instituto de Sistemas e Robótica
Av. Rovisco Pais
1049-001 Lisbon
Portugal

Abstract

This paper presents a multi-scale algorithm for the reconstruction of Human anatomy from a set of ultrasound images. Reconstruction is formulated in a Bayesian framework as an optimization problem with a large number of unknown variables. Human tissues are represented by the interpolation of coefficients associated to the nodes of a 3D cubic grid.

The convergence of the Bayesian method is usually slow and initialization dependent. In this paper, a multi scale approach is proposed to increase the convergence rate of the iterative process of volume estimation.

A coarse estimate of the volume is first obtained using a cubic grid with small number of nodes initialized with a constant value computed from the observed data. The volume estimate is then recursively improved by refining the grid step.

Experimental results are provided to show that multi-scale method achieves faster convergence rates compared with single scale approach. This is the key improvement towards real time implementations. Experimental results of 3D reconstruction of Human anatomy are presented to assess the performance of the algorithm and comparisons with the single scale method are presented.

Key words: medical imaging, 3D ultrasound, interpolation, multi-scale

1 Introduction

Three-Dimensional free-hand ultrasound aims to reconstruct the geometry and acoustic properties of Human organs from a set of ultrasound (US) images obtained during a clinical session. These images are associated to non parallel planes with known position and orientation [Quistgaard,(1997)], [Rohling et al.,(1996)]

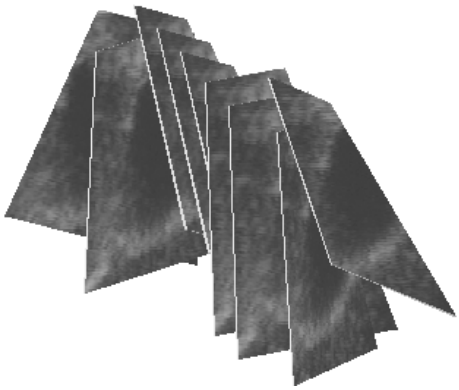

Fig. 1. US cross sections

(see Fig. 1). The reconstruction algorithm must be able to interpolate the data in regions which are not intersected by any inspection plane and must also be able to reduce the multiplicative noise associated to the observed images. Several algorithms have been proposed for 3D ultrasound imaging. These algorithms usually perform volume reconstruction in two steps [Nelson et al.,(1999)], [Carr,(1996)], [Steen et al.,(1994)], using a voxel representation of the region of interest (cuberille [Chen et al.,(1985)]). In the first step, voxels are filled with the data obtained from the inspection planes. In the second step, an average value is computed in the intersected voxels and an interpolation method is adopted to fill empty voxels.

3D reconstruction of medical objects has also been addressed in a Bayesian framework [Sanches et al.,(2000b)]. Reconstruction is formulated as an huge optimization problem where the unknown variables are to be estimated based on a set of incomplete and noisy data (US images). The images were obtained using a free-hand commercial ultrasound equipment with a spatial locator attached to the US probe [Pholhemus,(1993)]. In this way, the positions and orientations of the cross sections are stored together with the images and used during the estimation process. This approach has a sound theoretical basis and compare well with other reconstructions techniques as show in [Sanches et al.,(2000b)]. However, the Bayesian method exhibits a slow convergence rate.

This paper tries to overcome this difficulty by using a multi-scale strategy in the volume estimation.

First a rough estimate of the volume is obtained with a small number of parameters. The volume is approximated by an interpolation of the intensity values associated with a coarse cubic grid. Then the grid step is recursively reduced allowing to achieve more accurate estimates of the volume of interest.

This approach has two benefits. First it significantly reduces the computational time. The first iterations estimates a small number of coefficients (few dozens)

being therefore much faster. Only the last iterations optimize the objective function with respect to a large number of coefficients (millions). Therefore significant computational gain is achieved by using the multi scale approach.

Second, the use of low resolution descriptions in the first iterations allows a faster propagation of information along the 3D lattice which helps to overcome the problem of missing data in specific 3D regions.

2 Single Scale Algorithm

This section summarizes the MAP algorithm described in [Sanches et al.,(2000b)] used for a single scale (SS) description of the volume of interest.

The comparison of the method with other (e.g. [Nelson et al.,(1999)], [Carr,(1996)], [Treece et al.,(1999)], [Nelson et al.,(1997)], [Gee et al.(1999)]) is performed in [Sanches et al.,(2000b)]. It is concluded that the MAP method performs better but it is much slower.

The multi scale approach presented in section 3 will overcome this drawback.

Let f be a function describing the acoustic properties of the tissue in a given region of interest, $\Omega \subset R^3$.

It is assumed that f is a linear combination of basis functions (interpolation functions) $\phi_i : \Omega \rightarrow R$, i.e.,

$$f(x) = \Phi(x)^T U \tag{1}$$

where $\Phi(x) = [\phi_1(x), \phi_2(x), ..., \phi_N(x)]^T$ is a vector of basis functions and $U = [u_1, u_2, ..., u_N]^T$ is a Nx1 vector of coefficients which defines the volume of interest. The basis functions, $\phi_p(x)$ are obtained by shifting a function $h : R^3 \rightarrow R$ according to

$$\phi_p(x) = h(x - \mu_p) \tag{2}$$

where $\mu_p \in R^3$ are the nodes locations of a 3D cubic grid (see Fig. 2) defined in Ω and $h(x)$ is a tri-linear interpolation function defined by:

$$h(x) = \begin{cases} \prod_{k=1}^{3}(1 - \frac{|x^k|}{\Delta}) & x \in \delta \\ 0 & \text{otherwise} \end{cases} \tag{3}$$

where x^k is the k-th coordinate of x, $\delta = [-\Delta, \Delta]^3$ and Δ is the grid step.

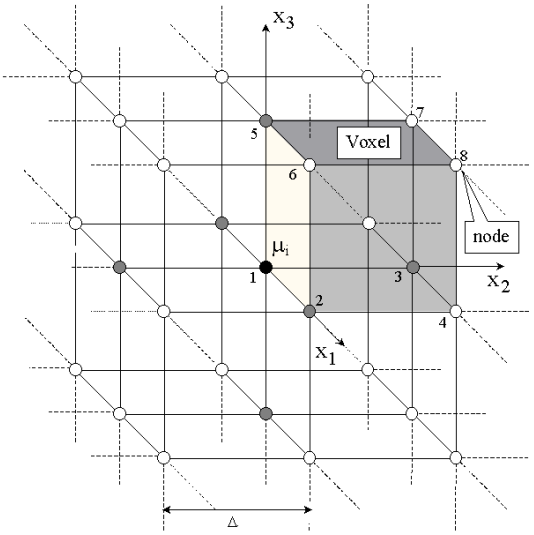

Fig. 2. 3D Grid and voxel representation.

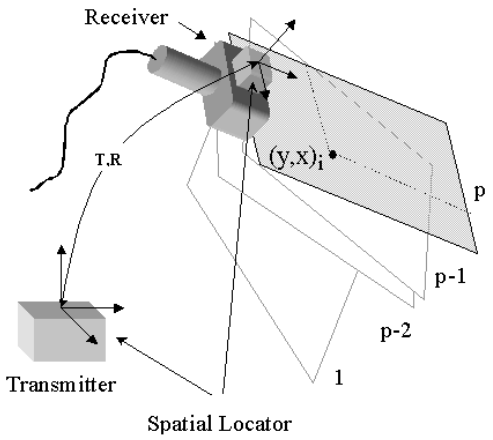

Fig. 3. Measurement of plane position and orientation.

A spatial locator is attached to the ultrasound probe (see Fig. 3). This allows to accurately measure the position and orientation of the inspection plane, provided that a careful calibration procedure is performed (e.g., see [Prager et al.,(1998)]). This allows to compute the 3D positions of the pixels associated with all the observed slices.

Therefore the available data is $V = \{y_i, x_i\}$ where y_i is the intensity of the i-th pixel and x_i is its corresponding 3D position. The 3D coordinates x_i are assumed to be accurately [1] known. Only the image intensities y_i are considered random variables. The 3D ultrasound problem aims the estimation of coefficients U, given V. This can be addressed using a MAP method as follows [Sanches et al.,(2000b)]

[1] The registering problem is not treated in this paper. This problem was published in [Sanches et al.,(2000a)], [Sanches et al.,(2002)].

$$\hat{U} = arg \max_{U} \ln(p(V|U)p(U)) \tag{4}$$

where $p(V|U)$ is the sensor model and $p(U)$ the prior density.

Suitable probability distribution must be defined for $p(V|U)$ and $p(U)$. This topic will be addressed below.

In this paper, pixel intensities are considered as independent random variables with a Rayleigh distribution leading to the likelihood function

$$p(V|U) = \prod_i \frac{y_i}{f(x_i)} e^{-\frac{y_i^2}{2f(x_i)}} \tag{5}$$

where f is the function to be retrieved.

These assumptions are not always true but they provide an acceptable model for the observed data which allow us to derive analytic expressions for the estimates. Several authors consider the pixel intensities as statistically independent [Dias et al.,(1996)] although the point spread function is sometimes greater than the inter pixel distance. The Rayleigh model is one of the model used in ultrasound imaging [Burckhardt,(1978)], [Abbot et al.,(1979)], [Wells et al.,(1981)] and it is assumed to be appropriate for the examples treated in this paper,

Intensity errors in US images are due to contructive/destructive interference phenomenon appearing in the ultrasound images as a kind of multiplicative noise (the US wave is a coherent radiation producing effects similar to those obtained in laser systems [Abbot et al.,(1979)], [Achim et al.,(2001)]). The Rayleigh model arises if the number of scatters per resolution cell is large, the echo complex magnitude components, in phase and quadrature, are normal distributed and the complex phase is uniformly distributed. When the number of scatters is small or some of them are stronger than the others (which happens in strong specular reflections associated to the organ boundaries) the Rayleigh model is no longer valid. In these cases other distributions should be used to describe the observed data (e.g., the K-distribution [Jakeman et al.,(1976)]). Furthermore, the ultrasound equipment usually perform a pre-processing of the raw data in order reduce the dynamic range of the RF signal for visualization purposes. This operation modifies the data distribution. However, it is possible to estimate the pre-processing function from the observed data and compensate the pre-process compression, obtaining an estimation of the original raw data [Sanches et al.,(2001)].

In this paper, it is assumed that the original data is described by the Rayleigh model and that the observed data is decompressed.

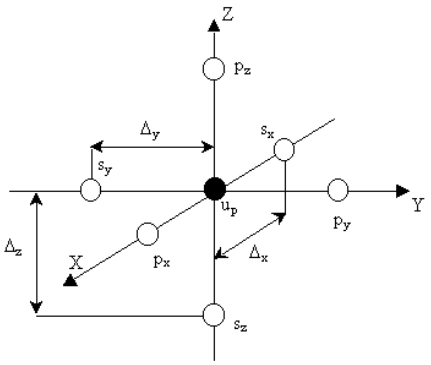

Fig. 4. Neighborhood representation.

The prior $P(U)$ plays an important role in the reconstruction process because it introduces a interpolation effect which allows to recover the function coefficients even when there is no data in its vicinity. This is the basic mechanism that allows to fill the volume gaps that were not intersected by any cross section. Furthermore, the prior also helps to avoid unstable behaviours during the optimization process [Katsaggelos,(1991)].

In this paper a Gaussian prior is used [Geman et al.,(1984)]

$$p(U) = \frac{1}{Z} e^{-\alpha \sum_{g \in G} \sum_{i \in \delta_g} (u_g - u_i)^2} \tag{6}$$

where G denotes the grid nodes, δ_g are the neighbors of the g-th node (see Fig.2), and Z is a normalization factor. This prior models the correlation among intensity coefficients on the volume of interest, Ω. In the Bayesian context, this prior takes into account the a priori knowledge about the volume to estimate. The adoption of this prior is equivalent to consider f as being bandwidth limited, i.e., neighboring nodes should have similar values.

This model depends on a parameter α which accounts for intensity changes between neighboring nodes. Each grid node is connected to 6 neighbors, except boundary nodes. The α parameter controls the strength of each connection. A high values of α correspond to imposing strong connections between neighboring nodes while low values of α correspond to imposing weak connections. Therefore, choosing large values of α leads to smooth estimates while small values of α leads to noisy estimates of the volume, with sharper transitions. The choice of α is a trade off between noise reduction and the ability to cope with intensity transitions. Furthermore, a high value of α allows to rapidly fulfill the gaps (i.e., regions which were not intersected by any cross section). In this paper the α parameter was obtained by trial and error and is sometimes modified during the estimation process, starting with high values being

gradually reduced.

The MAP reconstruction is the output of an optimization problem

$$\hat{U} = arg\max_{U} L(U) \tag{7}$$

where $L(U) = \ln(P(V/U)P(U))$ is the objective function to maximize. Using equations (5) and (6) we obtain

$$L(U) = \sum_{i} [\ln(\frac{y_i}{f(x_i)}) - \frac{y_i^2}{2f(x_i)}] - \alpha \sum_{g \in G} \sum_{i \in \delta_g} (u_g - u_i)^2 \tag{8}$$

The optimization of eqn (8) with respect to U is a difficult problem since the number of parameters to estimate is very large (typically millions of coefficients). Furthermore, $L(U)$ is a non convex and nonlinear function, for which there is no close form solution [Li,(1998)]. Therefore, numerical methods should be considered.

To solve eqn (7) the ICM algorithm proposed by Besag [Besag,(1986)] is used where the joint optimization problem is converted into a sequence of 1-dimensional optimization procedures. In each iteration, this method considers the objective function $L(U)$ as being a 1D function depending of a single parameter, keeping all the others constant. Along the iterative process all the parameters to estimate are updated sequentially until convergence is achieved.

Let $L(u_p)$ denote the objective function as a function of u_p coefficient, keeping all the others constant. To maximize $L(u_p)$, the following stationary condition must be met,

$$\frac{\partial L(u_p)}{\partial u_p} = 0 \tag{9}$$

After straightforward manipulation this leads to

$$\frac{1}{2} \sum_{i} \frac{y_i^2 - 2f(x_i)}{f^2(x_i)} \phi_p(x_i) + 2\alpha N_v (u_p - \bar{u}_p) = 0 \tag{10}$$

where N_v is the number of neighbors of u_p, $\phi_p(x_i)$ is the basis function associated to the p-th node computed at x_i and $\bar{u}_p = \frac{1}{N_v} \sum_{i \in \delta_p} u_i$ is the mean intensity associated to the p-th node neighbors .

This equation can be numerically solved by using the fixed point method [Press et al.,(1994)] leading to

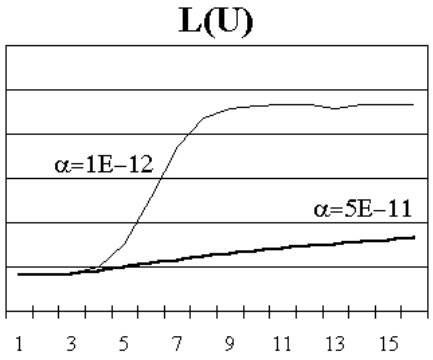

Fig. 5. Evolution of $L(U)$ along the iterative process for $\alpha = 10^{-12}$ and $\alpha = 5.10^{-11}$.

$$^{n+1}\hat{u_p} = \frac{1}{4\alpha N_v} \sum_i \frac{y_i^2 - 2f(x_i)}{f^2(x_i)} \phi_p(x_i) + \bar{u}_p \tag{11}$$

where $f(x)$ and $\bar{u}_p$ are computed by using the estimated values computed in the previous iteration.

3 Multi-Scale Algorithm

As it was stated before the Gibbs prior has a stabilization effect in the convergence process of the algorithm having, at the same time, a regularization effect in the final solution. This last effect can be controlled through the α parameter which plays a key role in enforcing the convergence of the algorithm as well as in reducing the multiplicative noise present in ultrasound images. However, the prior, leads to a decrease of the convergence rate of the optimization algorithm due to the propagation of information along the lattice nodes. This effect increases with the increase of α, since an increased dependence is enforced among neighboring nodes. Fig.5 shows the evolution of the objective function along the iterative process using synthetic data, for two different values of α, 10^{-12} and 5.10^{-11}. As shown, convergence rate for $\alpha = 5.10^{-11}$ is clearly smaller than for $\alpha = 10^{-12}$.

To overcome this difficulty [Herman et al.,(1999)], a multi-scale (MS) approach is proposed to speed up the convergence of the sequence defined in eqn (11).

The idea is simple. First we start with a low resolution grid (e.g. 8 nodes) and compute the node intensities for this grid. Then we increase the number of nodes during the optimization process until the final resolution is achieved. The initial volume for each resolution is computed from the final estimate obtained in the grid with lower resolution.

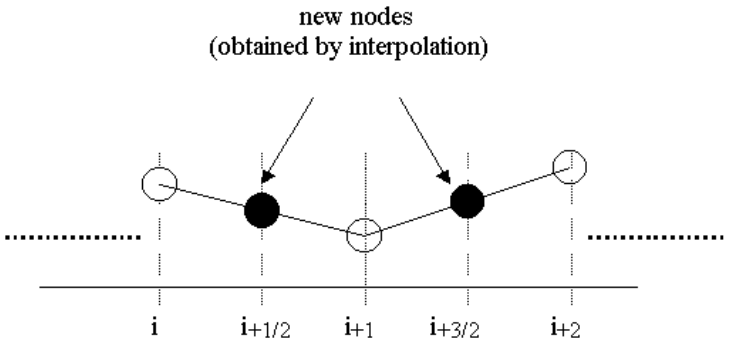

Fig. 6. Interpolation method to propagate the volume estimated in resolution grid n to the next resolution grid.

It will be shown that this strategy improves the convergence rate of the algorithm.

To implement this strategy it must be guaranteed that the objective function does not change during the grid refinement. This is achieved if the following conditions are met in every scale change (see appendix B):

- the resolution doubles from one grid resolution to the next, and
- the α parameter is proportional to the step of the grid.

The first condition guarantees that the vectorial spaces are nested, i.e, the nth vectorial space is a subset of the (n+1)th space. This is shown in appendix A. In this case, the ratio of discretization step in two consecutive scales is

$$r = \frac{\Delta^n}{\Delta^{n+1}} = 2 \tag{12}$$

where Δ^n and Δ^{n+1} are the steps associated to grids n and $n+1$ respectively. With this strategy of grid refinement the number of nodes per coordinate increases from two like $2, 3, 5, 9, 17, 33, 65, 129, ..., N, 2N-1, ...$ The initialization of the volume in the grid $n+1$ is easily computed from the estimated volume in grid n by keeping unchanged the nodes that already belong to n-th grid and interpolating between them to compute the value of the new ones, as shown in Fig.6.

To met the second condition, let us consider the simplest case in which grid step is the same for the three dimensions and equal to Δ^n for the highest and final resolution grid, and Δ^i for the grid step of one of the intermediate resolution grid. Let use, for each resolution grid i, different prior parameters defined as

$$\alpha_i = \frac{\Delta^i}{\Delta^n}\alpha, \qquad i = 1, .., n \tag{13}$$

Therefore the MS strategy is implemented as follows

1) The algorithm starts with a low resolution grid, e.g., $2 \times 2 \times 2$.
2) The i-th grid is obtained from the previous one by doubling its resolution (see eqn (12)). The nodes of the new grid are pre initialized with the values of $f(x)$ computed in the previous grid (see eqn (1)) at the locations of the new grid nodes (see Fig.6), i.e., $(u_p)_0^i = f_{i-1}(\mu_p^i)$, where μ_p^i is the 3D location of the u_p^i node.
3) For each grid the new estimation of U is obtained using eqn (11) where the α parameter is given by eqn (13).

In this way the objective function is invariant under grid refinements as required. Only one iteration is performed per grid scale during the first n iterations. The scale is then kept constant until a stop condition is met. The α parameter is used in eqn (13) is defined by the user and it is obtained by trial and error. It was concluded however that the reconstruction results are not strongly influenced by the choice of α when the multi scale approach is used.

In the first iteration each grid coefficient is initialize according to

$$u_p^0 = \frac{2\bar{y}^2}{\pi} \tag{14}$$

where $\bar{y}$ is the mean value of the observed data in the volume of interest Ω.

This estimate is derived from the expression of the expected value of a set of variables with Rayleigh distribution, $E(x) = \sqrt{\frac{\pi f}{2}}$.

The MS approach also simplifies the initialization procedure because only $8(2 \times 2 \times 2)$ nodes must be initialized. Furthermore, this initialization is always obtained from the observed data (see eqn 14), because, in the first resolution level (coarser grid), all nodes are intersected. On the contrary, in the SS method, the initialization procedure is more complex because it is necessary to adopt a strategy to fill the gaps corresponding to the nodes that were not intersected by any cross sections.

4 Experimental results

The multi-scale and single scale algorithm are evaluated based on three figures of merit: the a posteriori probability $L(U)$ (see eqn (7)), the signal to noise ratio of the reconstruction results, SNR and the number of iterations needed to achieve convergence.

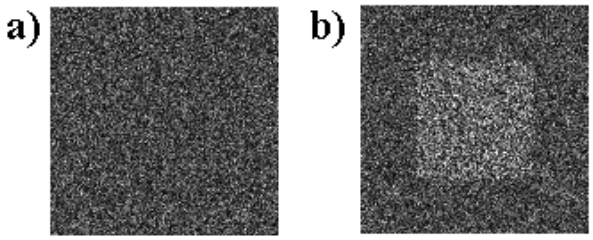

Fig. 7. Synthetic image with Rayleigh noise. a)background noise; b)cube intersection.

	$\alpha = 10^{-12}$		$\alpha = 5.10^{-12}$		$\alpha = 10^{-11}$	
	SS	MS	SS	MS	SS	MS
SNR(dB)	18.03	18.15	17.12	20.20	11.61	15.13
L(U)$\times 10^{-6}$	-8.277	-8.277	-8.302	-8.299	-8.313	-8.306

Table 1
Simulation results using a synthetic cube for $\alpha = 10^{-12}, 5.10^{-12}, 10^{-11}$.

Tree examples are presented. The first two examples use synthetic data, i.e.,cross sections extracted from a single cube or from a set of cubes. The third example uses a set of medical data corresponding to cross sections of a gall bladder.

In all these experiments a grid with $65 \times 65 \times 65$ nodes are used to reconstruct the data in the volume of interest. This means that 274625 coefficients have to be estimated. The reconstruction process is performed during fifteen iterations for the synthetic data and during twenty iterations for the medical data. From the figures representing the evolution of the objective function along the iterative process it is possible to conclude if convergence was or not was achieved and how far is from the convergence.

4.1 Example 1

The first set of tests uses a sequence of 50 parallel cross-sections extracted from a synthetic cube. Images with 128×128 pixels were computed by corrupting the cross sections with Rayleigh distributed noise. Fig.7 shows images corresponding to two different cross-sections: one extracted from the background and one intersecting the cube. The cube was reconstructed with the MAP algorithm for three values of α (α= 5.10^{-12}, 10^{-11}, 5.10^{-11}) after 15 iterations.

Figs.8-10 show the reconstruction results for $\alpha = 10^{-12}, 5.10^{-12}$ and 10^{-11} respectively. These figures show two cross sections of the reconstructed volumes using the SS and MS algorithms and the intensity profiles along the main

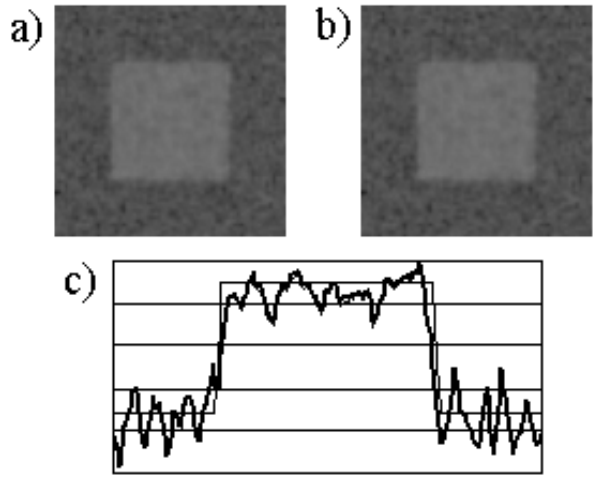

Fig. 8. Reconstruction results with $\alpha = 10^{-12}$:a,b) cross section extracted from the estimated volume obtained with SS algorithm and MS algorithm respectively. c)intensity profiles along the diagonal for the SS algorithm(thin line) and MS algorithm (thick line).

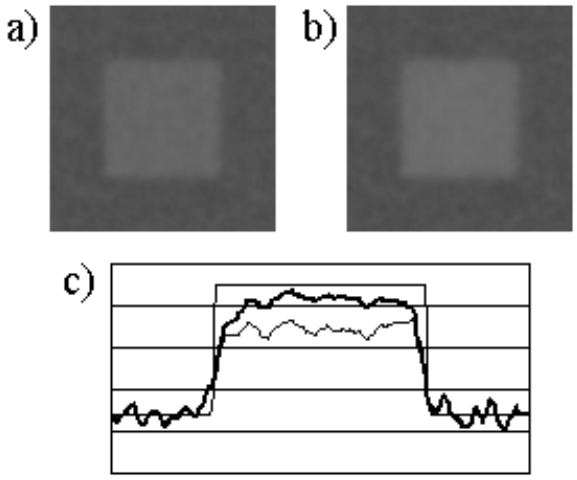

Fig. 9. Reconstruction results with $\alpha = 5.10^{-12}$:a,b) cross section extracted from the estimated volume obtained with SS algorithm and MS algorithm respectively. c)intensity profiles along the diagonal for the SS algorithm(thin line) and MS algorithm (thick line).

diagonal of the images.

Both methods provide similar results for small values of α ($\alpha = 10^{-12}$) but the reconstruction results become different for larger values of α.

Better results are always achieve by the MS method which shows a smaller bias.

This difference can also be observed in Table 1 which shows the SNR and the

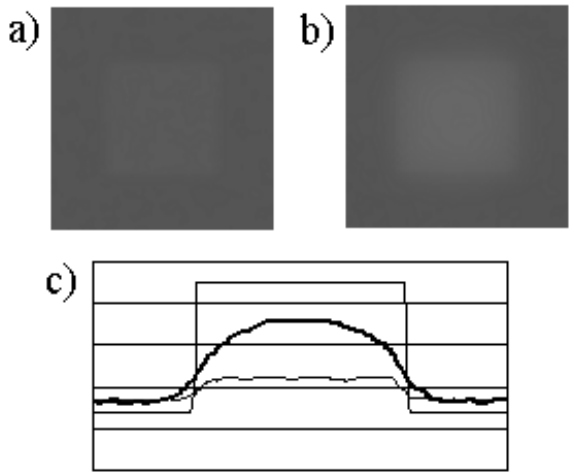

Fig. 10. Reconstruction results with $\alpha = 10^{-11}$:a,b) cross section extracted from the estimated volume obtained with SS algorithm and MS algorithm respectively. c)intensity profiles along the diagonal for the SS algorithm(thin line) and MS algorithm (thick line).

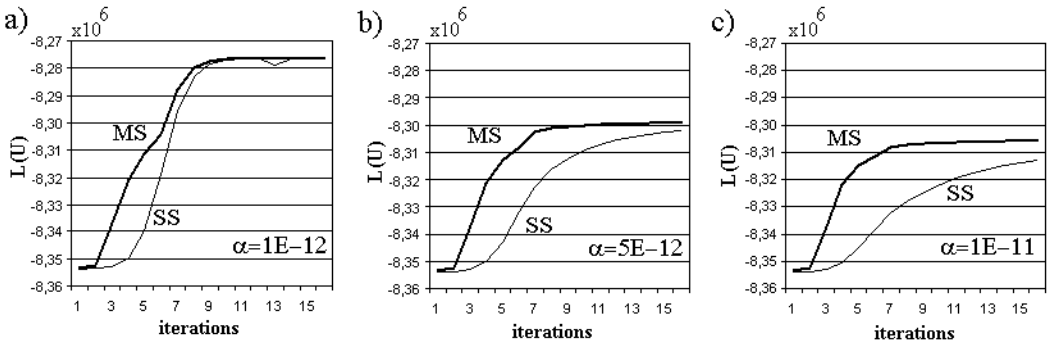

Fig. 11. Convergence of the single scale(SS) and multi scale(MS) algorithms. a)$\alpha = 10^{-12}$, b)$\alpha = 5.10^{-12}$, c)$\alpha = 10^{-11}$

$L(U)$ values for each experiment. The MS method achieves the best scores for all values of α.

Fig.11 represents the evolution of the objective function along the iterative process for both methods considering three values of α. It is visible from these figures that the MS approach converges faster than the SS algorithm achieving higher values of the objective function. The differences in the convergence rate are larger when the prior is stronger. Large values of α produce a long range smoothing which is easily propagated using the low resolution grid adopted in the first iterations of the MS method.

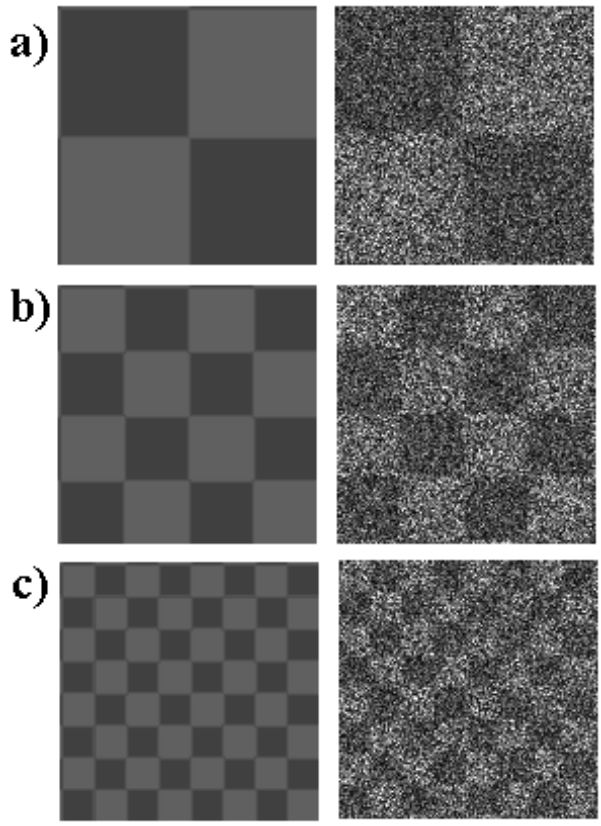

Fig. 12. Cross-sections extracted from three volumes with different number of transitions with no noise (upper row) and corrupted by Rayleigh noise (bottom row).

4.2 Example 2

Instead of considering an homogeneous cube as before, the volume of interest, Ω, is now filled with non overlapping cubes with two intensity levels. Three cases were considered ranging from a small number of cubes(8) to a high number of cubes(256) inside Ω.

Fig.12 shows three cross-sections extracted from the three volumes (left column) as well the corresponding images corrupted with Rayleigh noise (right column). Each volume was then reconstructed using $\alpha = 5.10^{-11}$ by both methods using 50 parallel cross sections of the volume of interest with 128×128 pixels.

Table 2 shows the SNR and L values obtained for each experiment. Better results are achieved by using the MS method as in the previous example.

This experiment also shows that the improvement obtained with the MS approach is data dependent. The improvement is higher when the number of transitions is small. This can be explained from the structure of the objec-

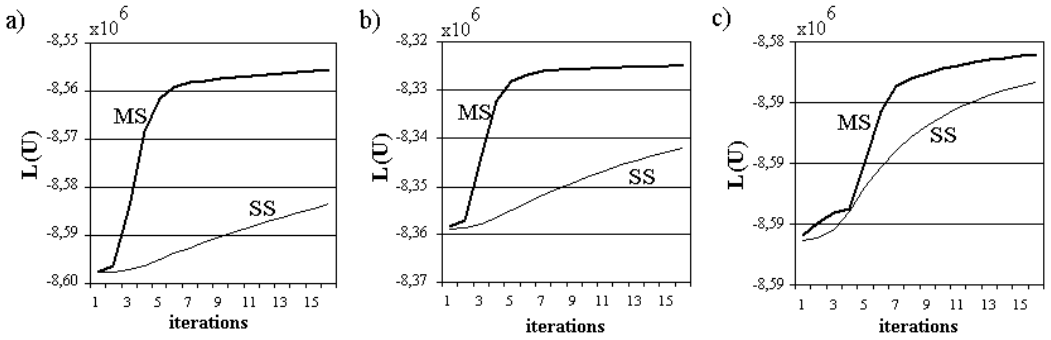

Fig. 13. Evolution of the objective function along the iterative process for three different original volumes with different number of transitions.

	8 Cubes		64 Cubes		256 Cubes	
	SS	MS	SS	MS	SS	MS
SNR(dB)	10.21	12.77	10.52	11.32	10.78	11.08
L(U)$\times 10^{-6}$	-8.58	-8.56	-8.34	-8.32	-8.59	-8.58

Table 2
Simulation results for three volumes filled with homogeneous cubes.

tive function L. The difference is more pronounced (2.5dB) when the volume exhibits large homogeneous regions which are better represented with small resolution scales. The multi-scale method allows to achieve reasonable reconstruction results, in this case, after the first two iterations, using low resolution models. This is not true when the volume of interest exhibits a large number of transitions. In this case higher resolution models are required to approximate the function f.

Fig.13 shows the evolution of the objective function along the optimization process. Faster convergence rates are obtained by the MS approach. The convergence rate of the MS approach does not depend on the experiment while the SS method converges slower when the volume of interest has large homogeneous regions(small number of transitions). It should also be stressed that each iteration in the MS scheme is faster than in the SS method, during the first stage of the optimization process corresponding to a computational gain.

4.3 Example 3

The experiments with real data were performed using a set of 62 images with 176×176 pixels corresponding to non-parallel cross-sections of a gall bladder obtained with an ultrasound probe. Fig.14a shows two ultrasound images belonging to the data sequence and the corresponding cross sections extracted

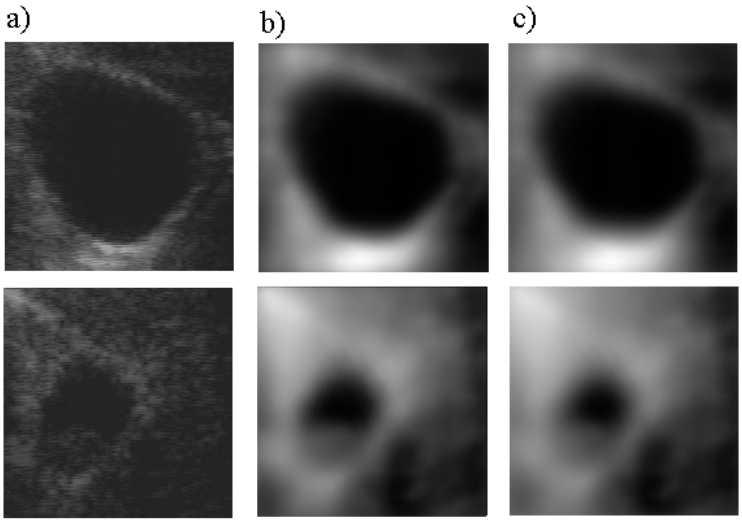

Fig. 14. a)Two cross sections belonging to the data set, b) and c) show the corresponding cross extracted from the estimated volumes using the SS and MS approach respectively.

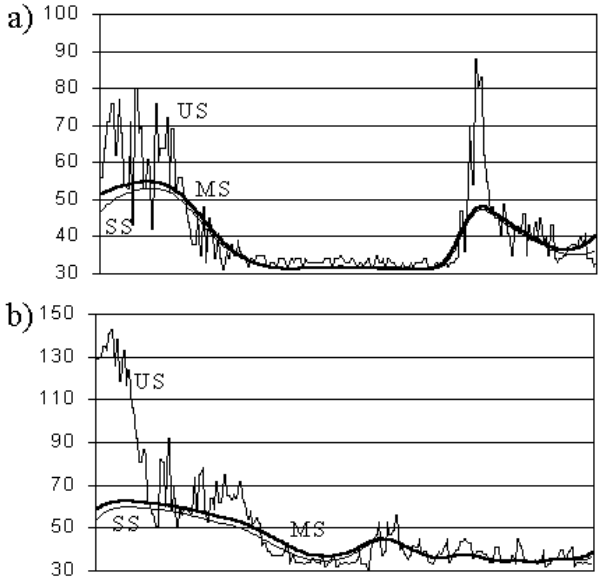

Fig. 15. Profiles extracted from the cross sections displayed in a)the first row and b)second row of Fig.14. US - Ultrasound image, SS-Reconstructed volume using the SS approach and MS-Reconstructed volume using the MS approach.

from the estimated volumes using the SS (Fig.14b) and MS (Fig.14c) approaches. Both methods lead to similar reconstructions results. However, the MS approach is faster and achieves a higher value for the objective function (see Fig.17). Fig.15 shows the main diagonal profiles extracted from the images displayed in Fig.14 and Fig.16 shows a 3D surface reconstruction of the gall bladder extracted from the estimated volume computed using the MS approach. This figure was obtained by applying a data segmentation algorithm

Fig. 16. Representation of the surface of the gall bladder extracted from the estimated volume using ray casting techniques.

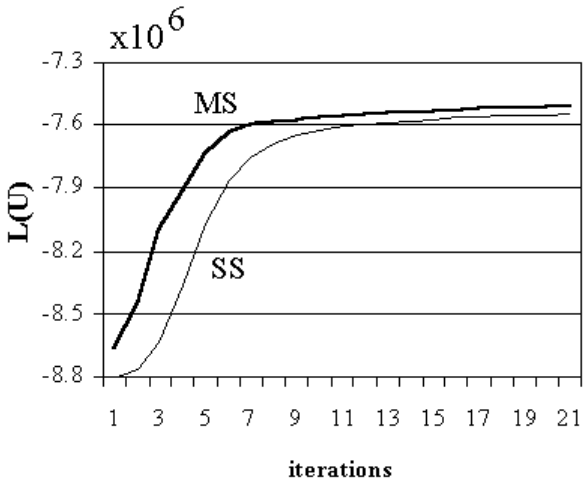

Fig. 17. Evolution of the objective function along the estimation iterative process of the gall bladder.

and using ray casting techniques.

The evolution of the objective function along the optimization procedure is displayed in Fig.17 for both methods (SS and MS).

5 Conclusions

This paper presents a Bayesian multi-scale algorithm for 3D reconstruction of Human organs from a set of ultrasound images. 3D data is approximated using a sequence of nested spaces with increasing resolution. Each space is spanned by a set of basis functions associated to the nodes of a cubic grid. An optimization method is proposed allowing to: i) estimate a linear combination of the basis functions for each resolution and to ii) predict the value of the coefficients in a space with higher resolution. These two steps alternate starting from a low resolution space until the desired resolution is achieved.

In this paper, volume reconstruction is performed using a set of cross sections of the region of interest. The position and orientation of each cross section are measured by a spatial locator sensor and therefore they are assumed to be known. This assumption is not always valid in practice. The 3D measurements provided by the Pholemus sensor used in this work are accurate. However, the pressure of the ultrasound probe against the human tissues causes geometric deformation which can not be omitted. This problem has been addressed by several authors [Nelson et al.,(1999)], [Treece et al.,(2001)], [Rohling et al.,(1998)] and by us in previous work[Sanches et al.,(2002)]. The methods described [Sanches et al.,(2002)] can be easily incorporated in the MS algorithm described here.

Experimental tests are presented to evaluate the algorithm with ultrasound data. It is concluded that the multi-scale concept leads to fast convergence rates. Convergence of the estimates using the MS method is achieved in less than 10 iterations, suggesting the possibility of using Bayesian estimation methods for interactive 3D ultrasound imaging.

The initialization procedure is also simplified using the MS method. In fact, only the 8 nodes of the coarsest grid (MS) must be initialized instead of the million nodes of the finest grid(SS). Initialization of these 8 nodes with a constant value, computed from the observed data, avoids the adoption of complex strategies to initialized the millions of nodes of the SS method, where some of them are not intersected by any cross-section.

Acknowledgment

This work was partially supported by FCT under project HEART 3D (SAPIENS). The ultrasound images were kindly provided by R. Prager and A. Gee from the University of Cambridge.

A Refinement

In this appendix we will show that doubling the resolution of the 3D grid leads to a sequence of nested vector spaces. Any function defined in a low resolution space can be easily expressed as a linear combination of the basis function associated to a high dimension space.

Consider a new 3D grid formed by a set of nodes at locations $\mu_\lambda = (x_0 + i\Delta_x/2, y_0 + j\Delta_y/2, z_0 + k\Delta_z/2)$, where (x_0, y_0, z_0) is the coordinate of the left-bottom corner of the region of interest(ROC).

To prove that the new set of base functions span a vectorial space that contains the older we just have to show that any basis function defined in the nth grid can be expressed as a linear combination of the basis functions defined in the (n+1)th grid.

Let

$$\phi_n^1(x) = h(x/\Delta_n^1) \tag{A.1}$$

be the first component of the basis function defined in the nth grid.

Thus

$$\phi_n(u) = \phi_n^1(u^1)\phi_n^2(u^2)\phi_n^3(u^3) \tag{A.2}$$

where $u = (u^1, u^2, u^3)$ and

$$h(x) = \begin{cases} \prod_{i=1}^{3}(1 - |x^i|) & x \in \delta \\ 0 & \text{otherwise} \end{cases} \tag{A.3}$$

We shall assume without lack of generality that $\phi_n^1(x)$, represented in Fig. A.1, is centered at the origin since any other base function can be obtained by simple shift it.

It is easy to show that (see Fig.A.1)

$$\phi_n^1(x) = \sum_{i=-1}^{1} \phi_n^1(i\frac{\Delta_n^1}{2})h(\frac{x - i\Delta_n^1/2}{\Delta_n^1/2}) \tag{A.4}$$

where $h(\frac{x-i\Delta_n^1/2}{\Delta_n^1/2}) = \phi_{(n+1)}^1(x - i\Delta_{(n+1)}^1)$ is the first component of the basis function defined in the (n+1)th grid and $\phi_n^1(i\Delta_n^1/2)$ is the value of the first

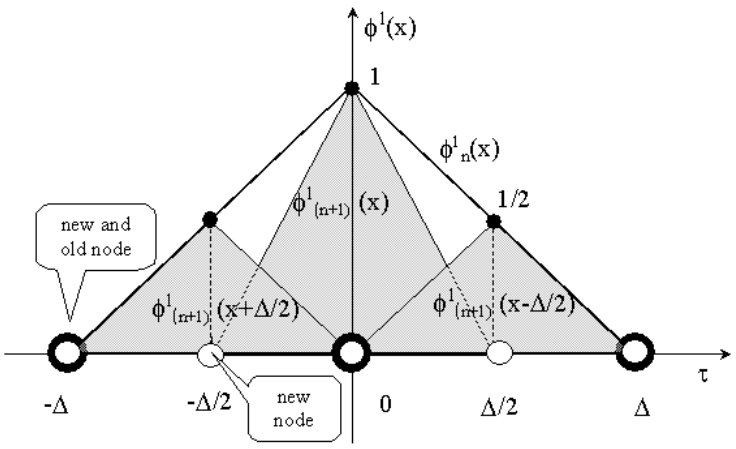

Fig. A.1. 1D Basis function.

component of the nth grid basis function calculated at the nodes of the (n+1)th grid. Replacing eqn (A.4) in eqn (A.2) leads to

$$\phi_n(u) = \sum_{i=-1}^{1} (\phi_n^1(\mu_i^1)\phi_{(n+1)}^1(u^1 - \mu_i^1)) \sum_{j=-1}^{1} (\phi_n^2(\mu_j^2)\phi_{(n+1)}^2(u^2 - \mu_j^2)) \sum_{k=-1}^{1} (\phi_n^3(\mu_k^3)\phi_{(n+1)}^3(u^3 - \mu_k^3)) \tag{A.5}$$

(A.6)

where $\mu_g = (\mu_i^1, \mu_j^2, \mu_k^3)$ is the position of the g-th node in the (n+1)th grid. After rearranging the terms the basis function defined in the nth grid can be written as follows

$$\phi_n(u) = \sum_{g=(i,j,k)} \phi_n(\mu_g)\phi_{(n+1)}(u - \mu_g) \tag{A.7}$$

Eqn (A.7) shows that a basis function defined in the nth grid can be obtained as a linear combination of the basis functions associated to the (n+1)th grid where the coefficients are the values of the nth grid basis function calculated in the positions of the nodes of the (n+1)th grid. This means that the space defined in the nth grid is nested in the space defined in the (n+1)th grid.

B Invariance of the objective function under grid refinement

Let us consider a general Gibbs distribution

$$P(f) = \frac{1}{Z} e^{-\alpha E(f)} \tag{B.1}$$

with energy defined by

$$E = \int\limits_{R \subset \Omega} \mid \nabla f(x) \mid^2 dv \tag{B.2}$$

where $f(x) = \sum_p u_p b_p(x)$.

Let us discretize this integral using a 3D grid with step $(\Delta^1, \Delta^2, \Delta^3.)$ The approximated value is

$$E \approx \sum_{p \in G} \mid \nabla f_d(x_p) \mid^2 \Delta^1 \Delta^2 \Delta^3 \tag{B.3}$$

where G is the set of all index of the grid and x_p is the 3D position of the p-th node.

The gradient can be approximated by first order backward differences,

$$\nabla f_d(x_p) = \begin{pmatrix} (u_p - s_1)/\Delta^1 \\ (u_p - s_2)/\Delta^2 \\ (u_p - s_3)/\Delta^3 \end{pmatrix} \tag{B.4}$$

where s_1, s_2, s_3 are the neighbors of u_p (see Fig. 4).

Substituting eqn (B.4) in eqn (B.3) leads to

$$E = \sum_p C_x (u_p - s_1)^2 + C_y (u_p - s_2)^2 + C_z (u_p - s_3)^2 \tag{B.5}$$

where $C_1 = \frac{\Delta_2 \Delta_3}{\Delta_1}, C_2 = \frac{\Delta_1 \Delta_3}{\Delta_2}$ and $C_3 = \frac{\Delta_1 \Delta_2}{\Delta_3}$.

When $\Delta_1 = \Delta_2 = \Delta_3 = \Delta$ eqn (B.5) takes the next form

$$E = \Delta \sum_p \sum_i (u_p - s_i)^2 \tag{B.6}$$

and substituting in eqn (B.1) leads to

$$P(U) = \frac{1}{Z} e^{-\alpha \Delta \sum_p \sum_i (u_p - s_i)^2} \tag{B.7}$$

Therefore, instead of using eqn (6) to define the prior to perform the MAP estimation we should use the eqn (B.7) that is a better approximation of eqn (B.5) which is independent of the discretization grid.

Furthermore, this approximation depends on the error by approximating $f(x)$ by $f_d^n(x)$ and the gradient $\nabla f(x)$ by eqn (B.4). However, in this case,

- since we are dealing with functions belonging to a finite dimension vectorial space (see eqn (1)) with linear derivatives with respect to the coefficients and
- the vectorial space associated to nth grid is nested in the vectorial space associated to the (n+1)th grid (as proved in appendix A)

then

$$E_d^n(U^n) = E_d^{n+1}(U^{(n+1)}) \tag{B.8}$$

where $E_d^n(U^n)$ and $E_d^{(n+1)}(U^{(n+1)})$ are the approximated discrete energies computed in nth and (n+1)th grids respectively.

Thus, our discrete energy, $E_d^n(U^n)$, that is to be maximized is kept constant under a grid refinement(q.e.d).

References

[Abbot et al.,(1979)] J. Abbot and F. Thurstone, Acoustic Speckle: Theory and Experimental Analysis, Ultrasound Imaging vol.1, pp.303-324, 1979.

[Achim et al.,(2001)] A.Achim, A.Bezerianos, P. Tsakalides, Novel Bayesian Multiscale Method for Speckle Removal in Medica Ultrasound Images, Trans. Medical Imaging, vol.20,no8,pp.772-783,August 2001.

[Besag,(1986)] J. Besag, On the Statistical Analysis of Dirty Pictures, J. R. Statist. Soc. B, vol.48, no. 3, pp. 259-302, 1986.

[Burckhardt,(1978)] C. Burckhardt, Speckle in Ultrasound B-Mode Scans, IEEE Trans. on Sonics and Ultrsonics, 25, n1, 1978.

[Carr,(1996)] Jonathan Carr, Surface Reconstruction in 3D Medical Imaging, Thesis presented for the degree of Doctor of Philosophy in Electrical and Electronic Engineering at the University of Canterbury, Christchurch, New Zealand, Fev. 1996.

[Chen et al.,(1985)] L.S.Chen, G.T.Herman, R.A.Reynolds, J.K.Udupa, Surface Shading in the Cuberille Environement, IEEE Computer Graphics and Applications, December 1985.

[Dias et al.,(1996)] J. Dias and J. Leitão, Wall position and thickness estimation from sequences of echocardiograms images, IEEE Transactions on Medical Imaging, vol.15, pp.25-38, February 1996.

[Herman et al.,(1999)] G.T.Herman, A.Kuba, Discrete Tomography, Foundations, Algorithms, and Applications, Birkhauser, 1999.

[Gee et al.(1999)] R. Rohling, A. Gee, L. Berman and G. Treece. Radial basis function interpolation for 3D freehand ultrasound. In Proceedings of the 16th International Conference on Information Processing in Medical Imaging, pages 478-483, Visegrd, Hungary, June 1999 (LNCS 1613, Springer).

[Geman et al.,(1984)] S. Geman and D. Geman, Stochastic Relaxation, Gibbs Distributions, and the Bayesian Restoration of Images, IEEE Trans on Pattern Analysis and Machine Intelligence, 6, 1984.

[Jakeman et al.,(1976)] E. Jakeman and P. N. Pusey, A Model for Non-Rayleigh See Echo, IEEE Transactions on Antennas and Propagation, Vol. AP-24, no.6, pp.806-814, November 1976.

[Katsaggelos,(1991)] A. K. Katsaggelos, Digital Image Restoration, Springer Series in Information Sciences, Springer-Verlag, 1991.

[Li,(1998)] S.Z.Li, Close-Form Solution and Parameter Selection for Convex Minimization-Based Edge-Preserving Smoothing, IEEE Trans. on PAMI, vol. PAMI-20, no.9, pp.916-932, September 1998.

[Nelson et al.,(1997)] T.R.Nelson, D.H.Pretorius, Interactive Acquisition, Analysis and Visualization of Sonographic Volume Data, International Journal of Imaging Systems and Technology, vol.8, pp.26-37, 1997.

[Nelson et al.,(1999)] T. Nelson, D. Downey, D. Pretorius, A. Fenster, Three-Dimensional Ultrasound, Lippincott, 1999.

[Pholhemus,(1993)] 3SPACE, Fasttrak, Users's Manual, Revision F, Polhemus, November 1993.

[Prager et al.,(1998)] R. W. Prager, R. N. Rohling, A. H. Gee, and L. Berman. Rapid calibration for 3-D freehand ultrasound. Ultrasound in Medicine and Biology, 24(6):855869, 1998.

[Press et al.,(1994)] W.H.Press, W.T.Vetterling, S.A.Teukolsky and B.P.Flanner, Numerical Recipes in C, Cambridge university press, 1994

[Quistgaard,(1997)] J. Quistgaard, Signal Acquisition and Processing in Medical Diagnostics Ultrasound, IEEE Signal Processing Magazine, vol14, n1, pp 67-74, 1997.

[Rohling et al.(1999)] R.N.Rohling, A. H. Gee and L. Berman, A comparation of freehand three-dimensional ultrasound reconstruction techniques, Medical Image Analysis, vol.4, no.4, pp.339-359, 1999.

[Rohling et al.,(1996)] R.Rohling and A. Gee, Issues in 3-D Free-Hand Medical Ultrasound Imaging, CUED/F-INFENG/TR 246, 1996.

[Rohling et al.,(1998)] R.N. Rohling, A.H. Gee and L. Berman, Automatic registration of 3-D ultrasound images, Ultrasound in Medicine and Biology, vol.24, no.6, pp.841-854, July 1998.

[Sanches et al.,(2000a)] J. Sanches, J. Marques, Alignment-by-Reconstruction for 3D Ultrasound Imaging, Proc. 15th ICPR, Barcelona, vol. 3, pp.41-44, September 2000.

[Sanches et al.,(2000b)] J. Sanches, J. Marques, A Rayleigh reconstruction/interpolation algorithm for 3D ultrasound, Pattern Recognition Letters, 21, pp.917-926, 2000.

[Sanches et al.,(2001)] J.Sanches, J. Marques, 3D Reconstruction from Log-Compressed Rayleigh Images, Proceedings International Conference on Image Processing, ICIP2001, Thessaloniki, Greece, October 2001.

[Sanches et al.,(2002)] J. Sanches, J. Marques, Joint Image Registration and Volume Reconstruction for 3D Ultrasound, Pattern Recognition Letters, Elsevier , 2002.

[Steen et al.,(1994)] E.Steen, B.Olstad, Volume Rendering of 3D Medical Ultrasound Data Using Direct Feature Mapping, IEEE Trans. on Medical Imaging, vol 13, n3,pp517-525, September 1994.

[Treece et al.,(1999)] G.M.Treece, R.W.Preager, A.H.Gee and L. Berman, Fast surface and volume estimation from non-parallel cross-sections, for frehand 3-D ultrasound, Medical Image Analysis, vol.3, no.2, pp.141-173, 1999.

[Treece et al.,(2001)] G. M. Treece, R. W. Prager, A. H. Gee and L. Berman. Correction of probe pressure artifacts in freehand 3D ultrasound. Proceedings of Medical Image Computing and Computer-Assisted Intervention (MICCAI 2001), pp. 283-290, Utrecht, The Netherlands, October 2001 (LNCS 2208, Springer).

[Wells et al.,(1981)] P.N.T. Wells, M.Halliwell, Speckle in ultrasonic imaging, Ultrasonics, September 1981.